analytical chemistry

Article

pubs.acs.org/ac

Visualization and Inhibition of Mitochondria-Nuclear Translocation of Apoptosis Inducing Factor by a Graphene Oxide-DNA Nanosensor

Yuhui Sun, Wen Gao,* Yujie Zhao, Wenhua Cao, Zhenhua Liu, Guanwei Cui, Lili Tong, Fengcai Lei, and Bo Tang*

College of Chemistry, Chemical Engineering and Materials Science, Collaborative Innovation Center of Functionalized Probes for Chemical Imaging in Universities of Shandong, Key Laboratory of Molecular and Nano Probes, Ministry of Education, Institute of Biomedical Sciences, Shandong Normal University, Jinan, Shandong 250014, P.R. China

Supporting Information

ABSTRACT: High concentrations of oxidized low density lipoprotein (oxLDL) induce aberrant apoptosis of vascular smooth muscle cells (VSMCs) in atherosclerotic plaques. This apoptosis cannot be blocked completely by the inhibition of caspase, and it eventually potentiates plaque disruption and risk for cardiovascular disease. Given the important role of apoptosis inducing factor (AIF) in caspase-independent apoptosis, here we develop an AIF-targeting nanosensor by the assembly of graphene oxide (GO) nanosheets and dye-labeled DNA hybrid structures. This nanosensor selectively localizes in the cytosol of VSMCs, where it exhibits a "turn-off" fluorescence signal. Under oxLDL stimuli, the release of AIF from mitochondria into cytosol liberates the DNA hybrid structures from the surface of GO and results in a "turn-on" fluorescence signal. This nanosensor is shown to possess rapid response, high sensitivity, and selectivity for AIF that enables real-time imaging of AIF translocation in VSMCs. Using this novel nanosensor, a better assessment of the apoptotic level of VSMCs and a more accurate evaluation of the extent of atherosclerotic lesions can be obtained. More importantly, the abundant binding between DNA hybrid structures and AIF inhibits the translocation of AIF into the nucleus and subsequent apoptosis in VSMCs. This inhibition may help stabilize plaque and reduce the risk of heart attack and stroke.

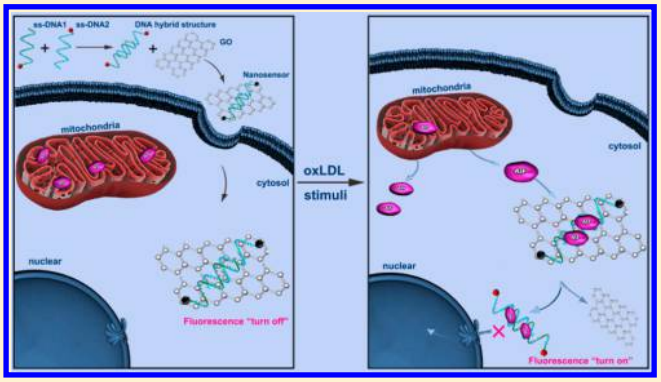

Cardiovascular disease and its complications are the primary cause of morbidity and mortality in modern society.[1] Atherosclerosis is distinguished by the formation of lipid-rich atherosclerotic plaques, which are at risk of rupture and underly many cardiovascular diseases.[2−4] High concentrations of oxidized low density lipoprotein (oxLDL) and its lipid constituents cause an increased apoptotic death rate of vascular smooth muscle cells (VSMCs) in primary lesions of atherosclerosis, gradually forming a "necrosis" area.[5−7] Apoptosis of VSMCs within established plaques can be harmful, which may potentiate vascular inflammation,[8,9] weaken the fibrous cap of the plaque, and eventually lead to the rupture of the plaque.[10−12] Thus, apoptosis is emerging as a principal pathophysiological mechanism of atherosclerosis.[13,14] Although caspase has been recognized as a key regulator of apoptosis, several lines of evidence demonstrate that blocking caspase activation only provides partial protection against aberrant apoptosis of VSMCs.[15−18] Therefore, other cell death mediators may be related to VSMC apoptosis.

Preliminary results have indicated that apoptosis inducing factor (AIF) is a type of flavoprotein involved in caspase-independent apoptosis, acting as a major early effector of cell death.[19,20] AIF appears to be a bifunctional protein with both an electron acceptor/donor (oxidoreductase) function and an independent apoptogenic function.[21,22] In healthy cells, AIF is expressed in the mitochondrial intermembrane space and possesses NADH oxidase activity.[23,24] However, AIF undergoes intracellular redistribution during treatment with apoptosis inducers and is released from mitochondria, via the cytosol, to the nucleus.[25,26] In the nucleus, AIF directly interacts with DNA, causing chromatin condensation and large scale DNA fragmentation (~50 kb) to exert its apoptotic function.[25,27] Given the important role of AIF in caspase-independent apoptosis, monitoring and regulating its translocation are critical for the aberrant apoptosis of VSMCs.

Current technologies for determining the subcellular localization of AIF mainly focus on transfection with AIF-GFP, immunocytochemistry, or Western blots, which are tedious and time-consuming processes,[28,29] together with poor sensitivity and specificity. Moreover, the main drawbacks of these methods are that they are not suitable for the real-time detection and regulation of AIF in living cells. Herein, we

Received: January 18, 2017
Accepted: March 31, 2017
Published: March 31, 2017

DOI: 10.1021/acs.analchem.7b00221
Anal. Chem. 2017, 89, 4642−4647

design and synthesize a simple, sensitive, and selective nanosensor for applications in both fluorescence activation imaging and inhibition of AIF translocation in living VSMCs (Scheme 1). This nanosensor consists of graphene oxide (GO)

Scheme 1. Illustration of the GO−DNA Nanosensor for the Visualization and Inhibition of AIF Translocation during Apoptosis

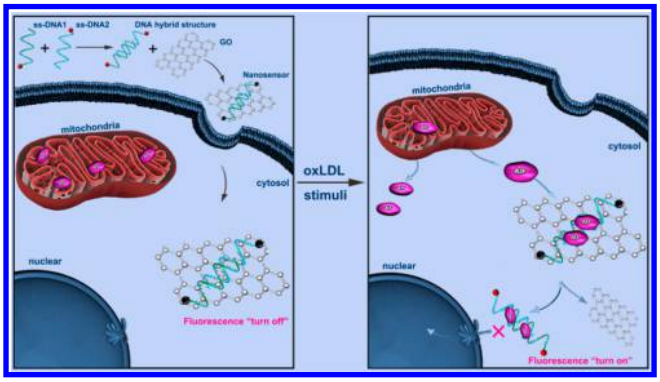

nanosheets that are conjugated with DNA hybrid structures. The DNA hybrid structure is composed of one double-stranded (ds) DNA body and two Cyanine (Cy5) dye labeled single-stranded (ss) DNA arms. The two ss-DNA arms and the GO nanosheets can integrate and assemble easily because of the $\pi-\pi$ stacking between them.[30−32] Due to the spatially selective localization of GO,[33−35] the as-fabricated GO−DNA nanosensor can be efficiently taken up by VSMCs into the cytosol rather than mitochondria and displays a "turn-off" fluorescence signal as a result of the superior quenching efficiency for the Cy5 on the GO surface. Under oxLDL stimuli, the release of AIF from mitochondria into the cytosol brings AIF and the nanosensor into close contact. AIF can bind with ds-DNA via a strong electrostatic interaction.[36,37] It allows the formation of a DNA hybrid structure−AIF complex along with the liberation of the DNA hybrid structure from the surface of GO nanosheet, resulting in a "turn-on" fluorescence signal. More importantly, the abundant formation of the DNA hybrid structure−AIF complex prevents the translocation of AIF into the nucleus and inhibits apoptosis of VSMCs. To the best of our knowledge, this is the first activatable nanosensor for "turn-on" fluorescence imaging of AIF translocation events as well as for impeding apoptosis processes in living VSMCs. Along with the above advantages, the nanosensor also has the potential to evaluate and possibly reduce the risk of atherosclerotic lesions.

EXPERIMENTAL SECTION

DNA Hybrid Structure Formation. The two ss-DNAs (ss-DNA1:5′-ACTCCTGGTACTCCTGTAATGAAGCGC-TAAGTGTAATGGAGAAGCGCTAA-3′-Cy5; ss-DNA2:3′-Cy5-GTGTAATGGAGAAGCGCTAATGAGGACCATGA-GGACATTACTTCGCGATT-5′, 1:1) were mixed in phosphate buffered saline (PBS: 1× phosphate, 137 mM NaCl, 2.7 mM KCl, pH 7.4), heated to 73 °C and maintained for 10 min, then slowly cooled to room temperature, and stored in the dark overnight to allow the formation of the double-stranded (ds) DNA body. The final concentration of the DNA hybrid structure was 20 μM.

Preparation of the GO−DNA Nanosensor. The GO nanosheets (500 μg) were first suspended in 1 mL of PBS (10× phosphate, pH 7.4) by ultrasonication for 30 min at room temperature, forming a GO stock solution for further use. The GO−DNA nanosensor was then prepared by adding 100 nM DNA hybrid structures to a solution of GO nanosheets (17.5 μg/mL) and then stirring for 20 min at room temperature in darkness. The prepared nanosensor was washed three times with PBS (10× phosphate, pH 7.4) and then redispersed in PBS (10× phosphate, pH 7.4) for further use.

Fluorescence Response to AIF. In selective and specific experiments, the GO−DNA nanosensor (17.5 μg/mL) was suspended in PBS (10× phosphate, pH 7.4), and AIF, PBS, Dulbecco's modified Eagles medium (DMEM), or the plasma extract of healthy VSMCs, as well as devitalized AIF, immunoglobulin G (IgG), bovine serum albumin (BSA), and human serum albumin (HSA) were examined. The concentration of each component was 35 μg/mL. The fluorescence was measured after 20 min at $\lambda_{ex}/\lambda_{em}$ = 648/668 nm. In sensitive experiments, 1.0 mL of GO−DNA nanosensor (17.5 μg/mL) was prepared in 2 mL microcentrifuge tubes, and then, different amounts (0, 5, 10, 15, 20, 25, 30, and 35 μg) of AIF were added. The measurements were performed as described above.

Confocal Imaging of AIF in Living Cells. Fluorescence imaging of AIF release in living VSMCs was performed as follows: VSMCs were plated on 20 mm glass bottom dishes (5×10^4 cells/dish) and cultured in FBS-free DMEM overnight and then incubated with sterilized GO−DNA nanosensor (17.5 μg/mL) at 37 °C for 4 h to permit cellular uptake of the nanosensor. After they were washed three times with PBS, the cells were incubated with the FBS-free DMEM containing oxLDL at a given concentration for an additional 90 min at 37 °C. Finally, the nucleus was counterstained with DAPI (10 mg/mL) for 5 min. Each well was washed three times with PBS before imaging with excitation at 405 and 633 nm by TCS SP8 confocal laser scanning microscopy.

Fluorescence imaging of the redistribution of AIF in living cells was implemented using the same method, except for an additional incubation step after oxLDL (60 μg/mL) induction, with 2 μM Mito@tracker (Rhodamine 123) for 20 min before imaging. Fluorescent images of the cells were examined at 488 and 633 nm.

Time-dependent fluorescence imaging of AIF translocation in living VSMCs was performed as follows: VSMCs were plated on 20 mm glass bottom dishes (5×10^4 cells/dish) and incubated with the GO−DNA nanosensor (17.5 μg/mL) in FBS-free DMEM for 4 h. The cells were then stained with DAPI (10 mg/mL) for 5 min. Fluorescence imaging was taken immediately after the addition of oxLDL (60 μg/mL). The real-time fluorescence images were collected every 5 min and monitored for 180 min. The photomultiplier tube smart gain and offset values were 556 and 0% for the blue channel and 845 and 0% for the red channel, respectively.

In the AIF nuclear translocation experiment, VSMCs were plated on 20 mm glass bottom dishes (5×10^4 cells/dish) and incubated with the GO−DNA hybrid structure nanosensor (17.5 μg/mL) in FBS-free DMEM for 4 h. After treating with 60 μg/mL oxLDL for an additional 300 min, the cells were counterstained with Hoechst 33342 (5 mg/mL) or Rhodamine 123 (2 μM). Fluorescent images of the cells were examined as described above.

AIF Protein Extraction and Western Blot Assay. Proteins of cytosol, mitochondria, and nucleus from VSMCs were extracted without modification according to the protocols

DOI: 10.1021/acs.analchem.7b00221
Anal. Chem. 2017, 89, 4642−4647

provided with the Cytoplasmic and Mitochondrial Protein Extraction Kit and the Nuclear and Cytoplasmic Protein Extraction Kit. All extractions from the given group were retained frozen at −80 °C before use. Equal amounts of protein (50 μg) were separated by 12% sodium dodecyl sulfate−polyacrylamide gel electrophoresis (SDS-PAGE), transferred to a PVDF membrane, and blocked with Tris buffered saline (TBS) containing 0.05% Tween-20 and 5% nonfat milk powder for 1 h. The membranes were then incubated with primary antibodies against AIF (1:1000) and β-actin (1:1000) overnight at 4 °C. After 3 washes with 1× TBST, the membranes were incubated with HRP-conjugated secondary antibody (1:50 000) for 1 h at room temperature. Detection was carried out by incubating the membranes for 5 min with the ECL reagent followed by imaging using a ChemiDoc Touch Imaging system (Bio-Rad, Hercules, CA, USA).

RESULTS AND DISCUSSION

Preparation and Characterization of GO−DNA Nanosensor. To prepare the nanosensor, single-layered GO nanosheets were selected, owing to their applications in intracellular imaging. After two Cy5-modified ss-DNA partly hybridized, the resulting DNA hybrid structure had one ds-DNA body and two ss-DNA arms. The DNA hybrid structure self-assembled on the surface of GO nanosheets via π−π stacking between two ss-DNA arms and GO nanosheets. The obtained GO−DNA nanosensor was characterized by dynamic light scattering (DLS) and atomic force microscopy (AFM) to study the changes in particle size and morphology during the synthesis. As shown in Figure S1, this nanosensor exhibited an average diameter of 141 ± 16 nm and a uniform thickness of 0.7 nm, which matched well with the typical lateral dimension and thickness for single-layered GO sheets. The successful synthesis of GO−DNA nanosensor was further confirmed by UV−vis-NIR spectra (Figure S2), which displayed characteristic absorption peaks of GO (238 nm) and Cy5-labeled DNA hybrid structure (DNA: 260 nm; Cy5 dye: 660 nm). Moreover, this nanosensor could be well-dispersed in PBS, fetal bovine serum (FBS), or cell medium without aggregation for 7 days at 4 °C (Figure S3).

In Vitro Response of GO−DNA Nanosensor. The fluorescence quenching efficiency of GO nanosheets was determined by fluorescence measurements of Cy5-labeled DNA hybrid structures (100 nM) in PBS (100 mM, pH 7.4) after adding different quantities of GO. The fluorescence was completely quenched within 3 min, suggesting a high fluorescence quenching ability for Cy5 by GO (Figure S4). We next sought to examine the fluorescence response of the nanosensor to the target AIF (Figure 1a). The fluorescence exhibited a significant recovery (~11-fold) after addition of 35 μg/mL of AIF, whereas in the presence of PBS, DMEM, or the plasma extract of healthy VSMCs, no characteristic fluorescence fingerprints were generated. These observations indicated that a high signal-to-background ratio can be obtained using the GO−DNA nanosensor without other interference in the components of the cell growth medium and the cell plasma. It was worth mentioning that free GO nanosheets display negative fluorescence responses to AIF, implying that the fluorescence "turn-on" was specific to the formation of a DNA hybrid structure−AIF complex that induced the liberation of the DNA hybrid structure from the surface of GO nanosheet. Gel electrophoresis analysis further confirmed this (Figure S5). Thus, when the nanosensor was incubated with the same

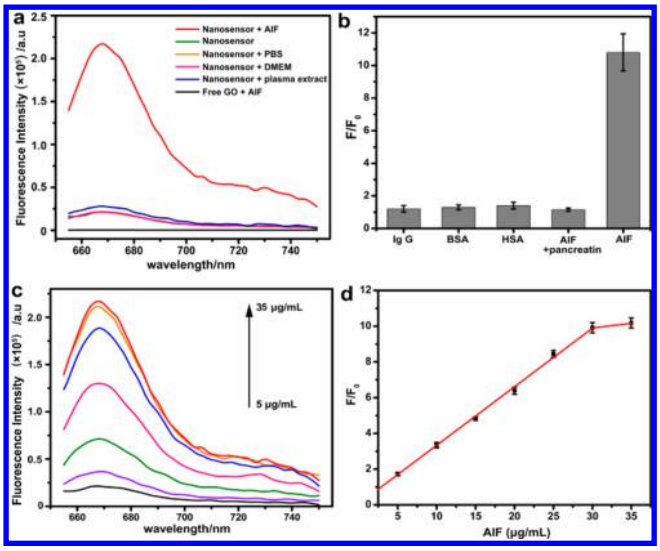

Figure 1. In vitro fluorescence response of the nanosensor to AIF. (a) Typical fluorescence spectra of the nanosensor (17.5 μg/mL) after adding AIF, PBS, DMEM, or the plasma extract of healthy VSMCs. (b) Fluorescence intensity changes (F/F_0) of the nanosensor toward different proteins. (c) Fluorescence spectra of the nanosensor (17.5 μg/mL) in the presence of different concentrations of AIF. (d) Enhanced fluorescence intensity (F/F_0) against the AIF concentration over the linear range of 5−30 μg/mL. Data are shown as mean ± SD of three independent experiments performed in duplicate.

amounts of devitalized AIF, immunoglobulin G (IgG), bovine serum albumin (BSA), and human serum albumin (HSA), no obvious fluorescence recovery was observed (Figure 1b). These data together verified that the nanosensor exhibited high selectivity and specificity for AIF and was unperturbed by other biologically relevant species. Figure 1c,d clearly showed a strong linear correlation (R = 0.9961) between the fluorescence intensity and the concentration of AIF, ranging from 5 to 30 μg/mL with a detection limit of 0.013 μg/mL. Fluorescence kinetic studies showed that the nanosensor responded to AIF in an instantaneous mode, achieving the maximum signal-to-noise ratio within 8 min. This rapid linear response remained unchanged even in the matrix of the cytoplasmic extract of healthy VSMCs (Figures S6 and S7), demonstrating the potential utility of this nanosensor for the real-time and quantitative imaging of AIF in apoptotic VSMCs.

Nuclease stability of the nanosensor was critical for the use of the nanosensor in living cells, and its nuclease resistance was evaluated using the enzyme deoxyribonuclease I (DNase I).[38,39] The fluorescence intensities of the nanosensor treated with or without DNase I remained at the baseline level. In contrast, incubation of the two solutions with AIF resulted in a marked enhancement of the fluorescence intensity (Figure S8), indicating that the nanosensor possessed a high resistance to nuclease and that the fluorescence recovery indeed occurred due to the formation of the DNA hybrid structure−AIF complex rather than to degradation by the nuclease. High concentration (70 μg/mL) or the long-term incubation of the nanosensor did not cause apparent cytotoxicity (Figure S9). These results demonstrated good biocompatibility of the nanosensor. Moreover, Hoechst staining to detect apoptosis clearly revealed that negligible apoptosis emerged, even after the VSMCs were incubated with the nanosensor (70 μg/mL) for 8 h (Figure S10). This result suggested that the nanosensor

DOI: 10.1021/acs.analchem.7b00221
Anal. Chem. 2017, 89, 4642−4647

did not induce apoptosis and can be used for VSMC apoptosis imaging.

Living Cell Imaging of AIF Release with GO−DNA Nanosensor. It has been reported that GO nanosheets and their conjugates can be internalized into the interior of cells.[40] We therefore investigated whether GO−DNA nanosensor would interact with and be internalized into VSMCs by using a photoacoustic (PA) imaging apparatus (based on the nanosensor with strong NIR absorption at 660 nm).[41] PA signal of VSMCs (10^5 cells in each sample) incubated with the nanosensor (17.5 μg/mL) demonstrated a significant internalization starting at 2 h and saturating at 4 h. To ensure sufficient uptake of the nanosensor in the cells, we chose a 4 h incubation period for the following cell assay. Moreover, employing PA imaging with multiple endocytosis inhibitors implied that the nanosensor was uptaken into VSMCs mainly through clathrin-mediated pathways (Figure S11). After investigation of the cellular uptake mechanism of the nanosensor, we next examined its ability for imaging of AIF release in VSMCs under oxLDL stimuli (Figure 2a). As expected, no distinct

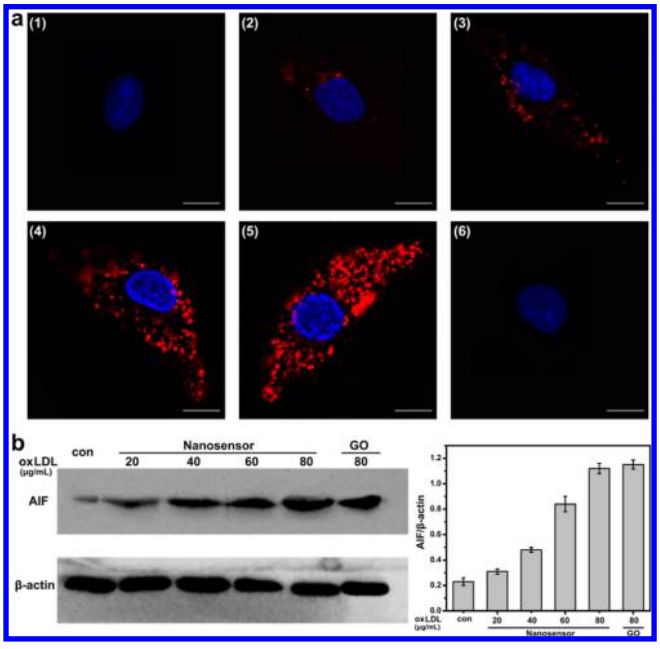

Figure 2. AIF release under apoptosis stimuli. (a) Fluorescence imaging of VSMCs preincubated with nanosensor (17.5 μg/mL) in serum-free DMEM medium for 4 h at 37 °C: (1) no treatment, (2) 20 μg/mL oxLDL for 90 min, (3) 40 μg/mL oxLDL for 90 min, (4) 60 μg/mL oxLDL for 90 min, (5) 80 μg/mL oxLDL for 90 min, and (6) preincubated with free GO for 4 h followed by 80 μg/mL oxLDL for 90 min. Scale bar = 5 μm. (b) Western blot analysis of plasma extracts from corresponding VSMCs. The AIF was normalized using β-actin. Data are shown as mean ± SD of three independent experiments performed in duplicate.

fluorescence signal was observed in nonapoptotic VSMCs, ascribed to the failure of the nanosensor to penetrate into the mitochondria and establish a distance to AIF. After the cells were subsequently treated with oxLDL at different concentrations (20, 40, 60, and 80 μg/mL) for 90 min, increasingly bright red fluorescence images were observed, especially at concentrations ≥60 μg/mL. This finding demonstrated higher concentrations of oxLDL could trigger the release of AIF from mitochondria along with an increasing accumulation in cytosol. In contrast, for VSMCs incubated with free GO followed by oxLDL (80 μg/mL) treatment, no visible fluorescence image was obtained. Immunofluorescence staining of these cells also revealed that cytosolic AIF (red, using antirabbit AIF as the primary antibody) increased in a oxLDL concentration-dependent manner (Figure S12). This finding was further supported by the assay of the plasma extracts in these cells using Western blotting and the nanosensor (Figures 2b and S13). These data together demonstrated that the nanosensor could be used as a sensitive and selective tool for the visualization of AIF that is released during VSMCs apoptosis. As the fluorescence intensity increased with the extent of apoptosis, the risk of atherosclerotic lesions could be evaluated.

We then verified the intracellular translocation of AIF during VSMC apoptosis. The release of AIF from mitochondria into the cytosol was evaluated by colocalization. The formation of the DNA hybrid structure−AIF complex liberated the DNA hybrid structure from the surface of the GO nanosheets and activated a "turn-on" fluorescence signal. Thus, the nanosensor with a high sensitivity for tracking AIF in living VSMCs could be implemented. Rhodamine 123 was used as a mitochondrial indicator.[42] As shown in Figure 3a, in nonapoptotic VSMCs, a

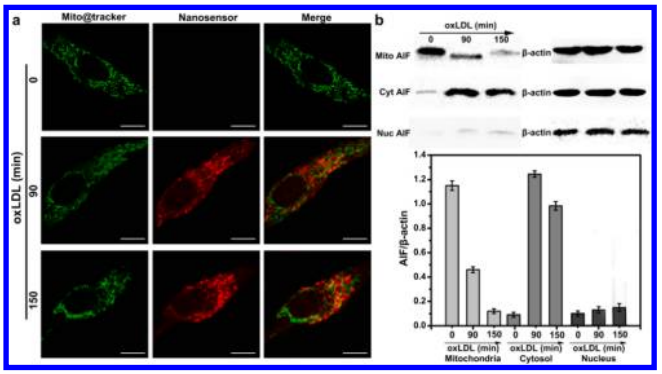

Figure 3. Translocation of AIF from mitochondria into the cytosol during apoptosis. (a) Fluorescence imaging of VSMCs incubated with nanosensor (17.5 μg/mL) in serum-free DMEM for 4 h, 60 μg/mL oxLDL for 0, 90, and 150 min, and 2 μM Mito@tracker (Rhodamine 123) for 20 min. Scale bar = 5 μm. (b) Western blot analysis of mitochondrial, cytosolic, and nuclear extractions from corresponding VSMCs. The AIF was normalized using β-actin. Data are shown as mean ± SD of three independent experiments performed in duplicate.

green fluorescence image was observed mainly in the space outside of the nucleus with a typical mitochondrial filamentous morphology.[43] This signal was not colocalized with the very weak red fluorescence signal for the nanosensor at the merge channel. After the cells were incubated with oxLDL (60 μg/mL) for 90 min, bright red fluorescence was uniformly distributed in the region of the mitochondria, while the green image showed that the mitochondria had not changed from a filamentous shape to a spherical shape. After 150 min, there was a notable increase in red fluorescence that was equally distributed in the cytosol between the mitochondria and the nucleus, and the mitochondria began to swell, which indicated the progression of cell apoptosis. Mitochondrial, cytosolic, and nuclear extractions were also prepared for Western blot analyses (Figure 3b), and a large amount of AIF accumulated in the mitochondria in the initial state and was accompanied by a corresponding increase in the cytosol during apoptosis. In addition, an immunofluorescence study was also performed to examine the distribution of AIF (Figure S14). This result was

DOI: 10.1021/acs.analchem.7b00221
Anal. Chem. 2017, 89, 4642−4647

further confirmed by assays of mitochondrial, cytosolic, and nuclear extractions using this nanosensor, and the recovery of fluorescence intensity was in accordance with the variation of AIF concentrations in mitochondria, cytosol, and nucleus (Figure S15). These results suggested that this nanosensor with high sensitivity and rapid fluorescence activation has been successfully used to track the release of AIF from mitochondria in living VSMCs.

Living Cell Imaging of AIF Nuclear Translocation for Apoptotic Studies. Because of its rapid response (<8 min), the nanosensor was capable of providing a platform for real-time visualization of AIF release in apoptotic VSMCs. The fluorescence images gave appreciable red after 30 min and reached the maximum intensity after 120 min for VSMCs that were treated with oxLDL (60 μg/mL) (Figure 4a), indicating

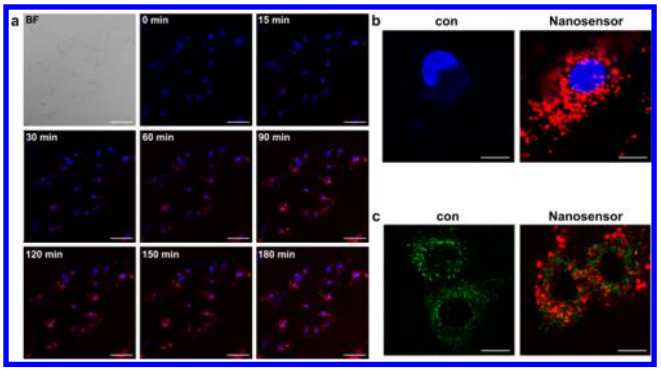

Figure 4. Real-time fluorescence imaging of VSMC apoptosis and studies of AIF nuclear translocation. (a) VSMCs incubated with 17.5 μg/mL nanosensor for 4 h followed by treatment with 60 μg/mL oxLDL; time-dependent fluorescence responses for the nanosensor were imaged. Scale bar = 25 μm. (b) Apoptosis-Hoechst staining of VSMCs incubated with the nanosensor (17.5 μg/mL) for 4 h, 60 μg/mL oxLDL for 300 min, and then Hoechst 33342 (5 mg/mL) for 10 min at 37 °C. Scale bar = 5 μm. (c) Colocalization fluorescence imaging of VSMCs incubated with the nanosensor (17.5 μg/mL) for 4 h, 60 μg/mL oxLDL for 300 min, and then 2 μM Mito@tracker (Rhodamine 123) for 20 min. Scale bar = 5 μm.

that the process of AIF release was quite slow and completed after nearly 2 h. This finding verified the previous reports that AIF release was slow in many cell types during apoptosis.[44−46] Moreover, by monitoring the fluorescence intensity of AIF during oxLDL stimuli over time, we found that the red fluorescence signal always remained in the cytosol from start to 180 min instead of translocating to the nucleus. We questioned whether the translocation of AIF from the cytosol to the nucleus could be impeded using this nanosensor. Hoechst staining showed that the nucleus in control VSMCs was severely shrunken and exhibited condensed apoptosis under oxLDL (60 μg/mL) stimuli for 300 min. In contrast, the nucleus in VSMCs pretreated with the nanosensor (17.5 μg/mL) was larger and displayed diffused chromatin (Figure 4b). Because mitochondrial fragmentation occurred in parallel with many modes of apoptosis,[47] colocalization of AIF with mitochondria was suggested to further demonstrate progression of VSMC apoptosis. As shown in Figure 4c, after incubating VSMCs with 60 μg/mL oxLDL for 300 min, the Mito@tracker image exhibited an obvious punctate pattern, which coincided with the apoptotic fragmentation of the mitochondria. However, in VSMCs that were pretreated with the nanosensor (17.5 μg/mL), a bright green fluorescence image indicated that the mitochondria were just beginning to change from filamentous to spherical, which was clear evidence of the slowdown of apoptosis. Furthermore, red fluorescence uniformly surrounded the nucleus, suggesting that the nanosensor had no influence on AIF activity and that the DNA hybrid structure−AIF complex blocked AIF nuclear translocation successfully. Immunofluorescence analysis of these cells also indicated that substantial AIF was visible in the nucleus in control VSMCs, while AIF in VSMCs that were pretreated with the nanosensor (17.5 μg/mL) was localized mainly in the space outside of the nucleus (Figure S16). These findings indeed verified that the nanosensor blocked AIF nuclear translocation and that inhibition of AIF nuclear translocation might inhibit aberrant apoptosis in VSMCs. This mechanism could possibly be used to reduce the risk of atherosclerotic plaque rupture.

CONCLUSIONS

In summary, by exploiting the high fluorescence quenching effectiveness of GO nanosheets toward DNA hybrid structures, we have successfully developed a novel AIF-targeting nanosensor. This nanosensor was synthesized rapidly via π−π stacking interactions between GO and the DNA hybrid structure, which offered high selectivity and sensitivity, as well as good stability and biocompatibility for both in vitro and intracellular detection of AIF. The resulting GO−DNA nanosensor enabled "turn-on" fluorescence imaging of AIF released from mitochondria in apoptotic VSMCs, and the fluorescence intensity revealed the extent of apoptosis. As the formation of DNA hybrid structure−AIF complex impaired the function of AIF entering the nucleus, the GO−DNA nanosensor could also significantly inhibit AIF nuclear translocation and aberrant apoptosis in VSMCs. Further efforts in the development of targetable, PEGylated sensors are expected to improve solubility and detection sensitivity and provide new opportunities for the precise imaging and effective inhibition of AIF translocation in atherosclerotic plaques. In view of these advantages and potentials, the developed GO−DNA nanosensor may be a powerful tool for accurate evaluation of the apoptotic level of VSMCs and the risk of atherosclerotic lesions, as well as for image-guided therapy of atherosclerosis by blocking aberrant VSMC apoptosis.

ASSOCIATED CONTENT

Supporting Information

The Supporting Information is available free of charge on the ACS Publications website at DOI: 10.1021/acs.analchem.7b00221.

Experimental details, DLS, AFM, UV−vis-NIR spectra, gel electrophoresis, fluorescence spectra, nuclease stability and cytotoxicity, PA imaging, and confocal fluorescence imaging (PDF)

AUTHOR INFORMATION

Corresponding Authors

*E-mail: tangb@sdnu.edu.cn.
*E-mail: gaowen@sdnu.edu.cn.

ORCID

Bo Tang: 0000-0002-8712-7025

Notes

The authors declare no competing financial interest.

DOI: 10.1021/acs.analchem.7b00221
Anal. Chem. 2017, 89, 4642−4647

■ ACKNOWLEDGMENTS

This work was supported by 973 Program (2013CB 933800) and National Natural Science Foundation of China (21390411, 21535004, 21227005, 21305081, 21575082, 21605097).

■ REFERENCES

(1) Anderson, K. M.; Odell, P. M.; Wilson, P. W.; Kannel, W. B. *Am. Heart J.* **1991**, *121*, 293−298.
(2) Hansson, G. K. *N. Engl. J. Med.* **2005**, *352*, 1685−1695.
(3) Thorp, E.; Cui, D.; Schrijvers, D. M.; Kuriakose, G.; Tabas, I. *Arterioscler., Thromb., Vasc. Biol.* **2008**, *28*, 1421−1428.
(4) Libby, P.; Ridker, P. M. *J. Am. Coll. Cardiol.* **2006**, *48*, A33−A46.
(5) Kataoka, H.; Kume, N.; Miyamoto, S.; Minami, M.; Morimoto, M.; Hayashida, K.; Hashimoto, N.; Kita, T. *Arterioscler., Thromb., Vasc. Biol.* **2001**, *21*, 955−960.
(6) Ding, Z.; Wang, X.; Schnackenberg, L.; Khaidakov, M.; Liu, S.; Singla, S.; Dai, Y.; Mehta, J. L. *Int. J. Cardiol.* **2013**, *168*, 1378−1385.
(7) Chen, J.; Mehta, J. L.; Haider, N.; Zhang, X.; Narula, J.; Li, D. *Circ. Res.* **2004**, *94*, 370−376.
(8) Kojima, Y.; Volkmer, J. P.; McKenna, K.; Civelek, M.; Lusis, A. J.; Miller, C. L.; Direnzo, D.; Nanda, V.; Ye, J.; Connolly, A. J.; Schadt, E. E.; Quertermous, T.; Betancur, P.; Maegdefessel, L.; Matic, L. P.; Hedin, U.; Weissman, I. L.; Leeper, N. J. *Nature* **2016**, *536*, 86−90.
(9) Libby, P.; Ridker, P. M.; Hansson, G. K. *Nature* **2011**, *473*, 317−325.
(10) Bennett, M. R.; Evan, G. I.; Schwartz, S. M. *J. Clin. Invest.* **1995**, *95*, 2266−2274.
(11) Clarke, M. C.; Figg, N.; Maguire, J. J.; Davenport, A. P.; Goddard, M.; et al. *Nat. Med.* **2006**, *12*, 1075−1080.
(12) Tabas, I. *Nat. Rev. Immunol.* **2010**, *10*, 36−46.
(13) Lutgens, E.; de Muinck, E. D.; Kitslaar, P. J.; Tordoir, J. H.; Wellens, H. J.; Daemen, M. J. *Cardiovasc. Res.* **1999**, *41*, 473−479.
(14) Schrijvers, D. M.; De Meyer, G. R.; Kockx, M. M.; Herman, A. G.; Martinet, W. *Arterioscler., Thromb., Vasc. Biol.* **2005**, *25*, 1256−1261.
(15) Okamura, T.; Miura, T.; Takemura, G.; Fujiwara, H.; Iwamoto, H.; Kawamura, S.; Kimura, M.; Ikeda, Y.; Iwatate, M.; Matsuzaki, M. *Cardiovasc. Res.* **2000**, *45*, 642−650.
(16) Abraham, M. C.; Shaham, S. *Trends Cell Biol.* **2004**, *14*, 184−193.
(17) Choudhury, S.; Bae, S.; Ke, Q.; Lee, J. Y.; Kim, J.; Kang, P. M. *Basic Res. Cardiol.* **2011**, *106*, 397−407.
(18) Choudhury, S.; Bae, S.; Kumar, S. R.; Ke, Q.; Yalamarti, B.; Choi, J. H.; Kirshenbaum, L. A.; Kang, P. M. *Cardiovasc. Res.* **2010**, *85*, 28−37.
(19) Susin, S. A.; Lorenzo, H. K.; Zamzami, N.; Marzo, I.; Snow, B. E.; Brothers, G. M.; Mangion, J.; Jacotot, E.; Costantini, P.; Loeffler, M.; et al. *Nature* **1999**, *397*, 441−446.
(20) Yuste, V.; Moubarak, R.; Delettre, C.; Bras, M.; Sancho, P.; Robert, N.; d'Alayer, J.; Susin, S. *Cell Death Differ.* **2005**, *12*, 1445−1448.
(21) Brown, D.; Yu, B. D.; Joza, N.; Benit, P.; Meneses, J.; Firpo, M.; Rustin, P.; Penninger, J. M.; Martin, G. R. *Proc. Natl. Acad. Sci. U. S. A.* **2006**, *103*, 9918−9923.
(22) Sun, H.; Yang, S.; Li, J.; Zhang, Y.; Gao, D.; Zhao, S. *Biochem. Biophys. Res. Commun.* **2016**, *472*, 137−143.
(23) Delettre, C.; Yuste, V. J.; Moubarak, R. S.; Bras, M.; Lesbordes-Brion, J. C.; Petres, S.; Bellalou, J.; Susin, S. A. *J. Biol. Chem.* **2006**, *281*, 6413−6427.
(24) Joza, N.; Susin, S. A.; Daugas, E.; Stanford, W. L.; Cho, S. K.; Li, C. Y.; Sasaki, T.; Elia, A. J.; Cheng, H. Y.; Ravagnan, L.; Ferri, K. F.; Zamzami, N.; Wakeham, A.; Hakem, R.; Yoshida, H.; Kong, Y. Y.; Mak, T. W.; Zúñiga-Pflücke, J. C.; Kroemer, G.; Penninger, J. M. *Nature* **2001**, *410*, 549−554.
(25) Wang, X.; Yang, C.; Chai, J.; Shi, Y.; Xue, D. *Science* **2002**, *298*, 1587−1592.
(26) Cande, C.; Vahsen, N.; Garrido, C.; Kroemer, G. *Cell Death Differ.* **2004**, *11*, 591−595.
(27) Lorenzo, H. K.; Susin, S. A.; Penninger, J.; Kroemer, G. *Cell Death Differ.* **1999**, *6*, 516−524.
(28) Yu, S. W.; Wang, H.; Poitras, M. F.; Coombs, C.; Bowers, W. J.; Federoff, H. J.; Poirier, G. G.; Dawson, T. M.; Dawson, V. L. *Science* **2002**, *297*, 259−263.
(29) Zhang, W.; Wang, X.; Chen, T. *Mol. Cell. Biochem.* **2011**, *354*, 29−37.
(30) He, S.; Song, B.; Li, D.; Zhu, C.; Qi, W.; Wen, Y.; Wang, L.; Song, S.; Fang, H.; Fan, C. *Adv. Funct. Mater.* **2010**, *20*, 453−459.
(31) Manohar, S.; Mantz, A. R.; Bancroft, K. E.; Hui, C. Y.; Jagota, A.; Vezenov, D. V. *Nano Lett.* **2008**, *8*, 4365−4372.
(32) Li, F.; Feng, Y.; Zhao, C.; Li, P.; Tang, B. *Chem. Commun.* **2012**, *48*, 127−129.
(33) Chen, T. T.; Tian, X.; Liu, C. L.; Ge, J.; Chu, X.; Li, Y. *J. Am. Chem. Soc.* **2015**, *137*, 982−989.
(34) Wang, H.; Zhang, Q.; Chu, X.; Chen, T.; Ge, J.; Yu, R. *Angew. Chem., Int. Ed.* **2011**, *50*, 7065−7069.
(35) Li, L.; Feng, J.; Liu, H. Y.; Li, Q. L.; Tong, L. L.; Tang, B. *Chem. Sci.* **2016**, *7*, 1940−1945.
(36) Candé, C.; Cecconi, F.; Dessen, P.; Kroemer, G. *J. Cell Sci.* **2002**, *115*, 4727−4734.
(37) Ye, H.; Cande, C.; Stephanou, N. C.; Jiang, S.; Gurbuxani, S.; Larochette, N.; Daugas, E.; Garrido, C.; Kroemer, G.; Wu, H. *Nat. Struct. Biol.* **2002**, *9*, 680−684.
(38) Seferos, D. S.; Prigodich, A. E.; Giljohann, D. A.; Patel, P. C.; Mirkin, C. A. *Nano Lett.* **2009**, *9*, 308−311.
(39) Gao, W.; Cao, W. H.; Sun, Y. H.; Wei, X. P.; Xu, K. H.; Zhang, H. B.; Tang, B. *Biomaterials* **2015**, *69*, 212−221.
(40) Jiang, T. Y.; Sun, W. J.; Zhu, Q. W.; Burns, N. A.; Khan, S. A.; Mo, R.; Gu, Z. *Adv. Mater.* **2015**, *27*, 1021−1028.
(41) Wang, Y. W.; Fu, Y. Y.; Peng, Q. L.; Guo, S. S.; Liu, G.; Li, J.; Yang, H. H.; Chen, G. N. *J. Mater. Chem. B* **2013**, *1*, 5762−5767.
(42) Gao, W.; Xu, K.; Ji, L.; Tang, B. *Toxicol. Lett.* **2011**, *205*, 86−95.
(43) Karbowski, M.; Youle, R. *Cell Death Differ.* **2003**, *10*, 870−880.
(44) Norberg, E.; Gogvadze, V.; Ott, M.; Horn, M.; Uhlén, P.; Orrenius, S.; Zhivotovsky, B. *Cell Death Differ.* **2008**, *15*, 1857−1864.
(45) Deng, Y.; Ren, X.; Yang, L.; Lin, Y.; Wu, X. *Cell* **2003**, *115*, 61−70.
(46) Arnoult, D.; Gaume, B.; Karbowski, M.; Sharpe, J. C.; Cecconi, F.; Youle, R. J. *EMBO J.* **2003**, *22*, 4385−4399.
(47) Green, D. R.; Kroemer, G. *Science* **2004**, *305*, 626−629.

DOI: 10.1021/acs.analchem.7b00221
Anal. Chem. 2017, 89, 4642−4647